ACS OMEGA

http://pubs.acs.org/journal/acsodf

Article

Catalpol Research on the Mechanism of Antimyocardial Reperfusion Injury by Regulating the MiR-126/TWEAK-FN14 Pathway: In Vitro and Computer Simulation Studies

Ting Wang,[†] Chongyu Shao,[†] Huiyan An, Guanfeng Xu, Haitong Wan,* and Jiehong Yang*

Cite This: *ACS Omega* 2025, 10, 19538−19551

ABSTRACT: The objective of this study was to investigate the mechanism through which catalpol (CAT) exerts its protective effects in the context of myocardial ischemia-reperfusion injury. Preliminary results showed that Cat significantly attenuated oxygen-glucose deprivation/reoxygenation (OGD/R) damage to H9C2 cells, inhibited intracellular reactive oxygen species levels, and downregulated the protein expression of TWEAK and Fn14 post-OGD/R. The intracellular level of miR-126 was downregulated after OGD/R, and this effect was reversed by CAT administration. To further elucidate its mechanisms, a miR-126 inhibitor was used in the H9C2 cells, and the inhibitory effect was validated using real-time fluorescence quantitative polymerase chain reaction (RT-PCR). Following CAT treatment, lactate dehydrogenase (LDH) levels within the cells were assessed. The results revealed that CAT not only decreased LDH levels but also modulated the miR-126/TWEAK-FN14 signaling axis and the expression of inflammatory-related mediators, as evidenced through RT-PCR and Western blot. Additionally, molecular docking (MD) studies suggested that CAT exhibited a strong binding affinity to both the signaling pathway and inflammatory-related components. Furthermore, molecular dynamics simulations (MDS) demonstrated that the CAT-protein complex exhibited high stability, flexibility, and low binding free energy under physiological conditions. Additionally, CAT showed favorable absorption, distribution, metabolism, excretion, and toxicity characteristics. In summary, this study, through in vitro experimentation, confirmed that CAT regulates the miR-126 and inflammatory proteins within the signaling pathway, with these results being further supported by MD and MDS analyses.

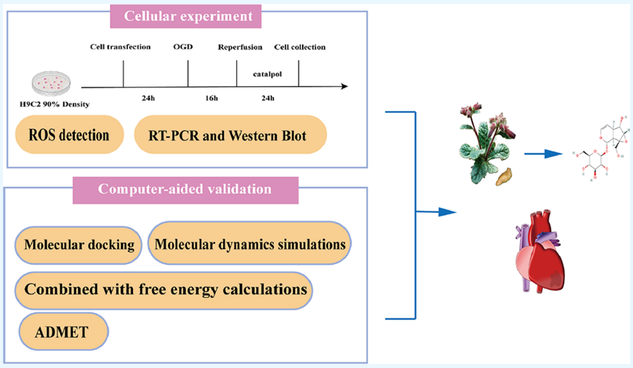

1. INTRODUCTION

Myocardial infarction (MI), commonly referred to as a heart attack, is a leading cause of mortality worldwide. The World Health Organization reports that approximately 17 million people succumb to cardiovascular diseases each year, with over one-third of these fatalities resulting from myocardial infarction.[1,2] This condition arises when the coronary arteries become obstructed, causing a lack of oxygen and a reduced supply of nutrients to the heart muscle, which can lead to cell death through necrosis. The necrotic myocardial cells then release cytokines, including TNF-α.[3] In clinical settings, the treatment of myocardial infarction often involves a combination of antiplatelet agents, anticoagulants, beta-adrenergic antagonists, ACE inhibitors, angiotensin receptor blockers (ARBs), and statins. These pharmaceuticals are instrumental in mitigating thrombotic events, easing the cardiac workload, and reducing the extent of myocardial ischemia.[4] However, many of these drugs are associated with significant side effects, such as gastrointestinal discomfort, bleeding, depression, and renal dysfunction.[5,6] Given these challenges, there is an urgent need to investigate safer and more effective alternative treatments for myocardial infarction.

Catalpol(CAT), an active compound derived from Rehmannia, showcases a variety of pharmacological effects, including anti-inflammatory, antioxidant, and antiapoptotic properties.[7−9] It has been demonstrated to mitigate the inflammatory response in reperfusion injury by inhibiting the release of pro-inflammatory mediators. Studies indicate that CAT prevents the nuclear translocation of NF-κB/p65 and reduces TNF-α,[10] thereby alleviating the myocardial inflammatory response associated with ischemia-reperfusion. Fur-

Received: January 5, 2025
Revised: March 20, 2025
Accepted: April 16, 2025
Published: May 9, 2025

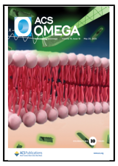

https://doi.org/10.1021/acsomega.4c11357

thermore, the NLRP3 inflammasome plays a significant role in numerous inflammatory diseases, including rheumatoid arthritis, systemic lupus erythematosus, diabetes, and obesity-related inflammation.[11−15] CAT has been shown to inhibit the assembly and activation of the NLRP3 inflammasome, resulting in reduced secretion of inflammatory factors and underscoring its anti-inflammatory potentiality.[16]

miR-126 is an essential microRNA (miRNA) that plays a protective role in endothelial cells by regulating various target genes, effectively mitigating inflammation and oxidative stress.[17−19] In the context of cardiovascular diseases, the expression of miR-126 is frequently reduced.[20,21] TWEAK and its receptor, Fn14, are involved in numerous physiological and pathological processes, including apoptosis, inflammation, and regeneration.[22,23] The excessive activation of the TWEAK/Fn14 pathway in cardiovascular diseases is closely associated with endothelial cell damage, inflammation, and myocardial injury.[24,25]

Yin et al. discovered that the Fuzheng Liqi formula significantly reduces TWEAK levels associated with cachexia.[26] Rehmannia, which contains the key component CAT is believed to play an essential role in regulating TWEAK levels. Therefore, we speculate that CAT may modulate the pathway TWEAK/FN14 through miR-126, thereby attenuating the inflammatory response after OGD/R. The research employed H9C2 to investigate the anti-inflammatory properties of CAT and to clarify the involved signaling pathways. To bolster our findings, molecular docking(MD), molecular dynamics simulations (MDS) and absorption, distribution, metabolism, excretion, and toxicity (ADMET) predictions techniques were utilized in conjunction with in vitro experiments. Ultimately, the findings indicate that CAT has a significant effect on the inflammatory response in H9C2 myocardial cells following oxygen-glucose deprivation/reoxygenation (OGD/R).

2. MATERIALS AND METHOD

2.1. Materials. CAT (Cat No: 2415−24−9) was obtained from Chengdu Effbio Biotechnology Co., Ltd. (Chengdu, China). The Cell Counting Kit-8 (Cat No: BS350B) was acquired from Wu Han Seari Biotech. The LDH Cytotoxicity Assay Kit (Cat No: C0018M) was sourced from Beyotime Biotechnology (Shanghai, China), and the Fastpure Cell/Tissue Total RNA Isolation Kit was supplied by Vazyme (Nanjing, China). The RNA Transfection Reagent (Cat No: E607402−1000) was purchased from Shanghai GenePharma, Ltd.Additionally, the following products were sourced from Hunan Ag bio Biotechnology: the miRNA cDNA First Strand Synthesis Kit (stem-loop method) (Cat No: AG11743), Evo M-MLV Reverse Transcription Premix (Cat No: AG11706), and SYBR Green Pro Taq HS Premix qPCR Kit (with ROX). TWEAK (Cat No: 336C6A19) was procured from INVITROGEN, while FN14 (Cat No: ET1611−93) was obtained from Hua An Biological. NLRP3 (Cat No: HY-P80246) was sourced from MCE. Lastly, the following items were purchased from Abmart Pharmaceuticals Technology. (Shanghai): TNF-α (Cat No: PY19810), NF-κB P65 (Cat No: TA5006), NF-κB P−P65 (Cat No: TA2006), and β-actin (Cat No: TP70753).

2.2. Databases, Websites, and Software. GeneCards-(http://www.genecards.org), UniProt (https://www.uniprot.org), STRING (http://stringdb.org/cgi/input.pl), Metascape-(https://metascape.org/gp/index.html#/main/step1), PubChem(.https://pubchem.ncbi.nlm.nihgov/), AlphaFold-(https://www.alphafold.ebi.ac.uk/), Acpype Server(https://www.bio2byte.be/acpype/), Cytoscape 3.9.1 software, DruLiTor software, AutoDockTools 1.5.6 software, AutoDock Vina 1.2.3 software, PyMOL 2.5 software, Discovery Studio Visualizer 2021 software, ORCA 5.0.4 software, Multiwfn 3.8 software, Gromacs 2022.2, Gromacs 2023, and Gmx_MMPBSA software.

2.3. Cell Culture. H9C2 cells (Accession Number: CL-0089)were obtained from Procell Life Sciences (Wuhan, China) and were cultured in a 37 °C constant temperature incubator with 5% CO_2 concentration, using DMEM medium containing 10% fetal bovine serum.

2.4. Establishment of an OGD/R Model. For the experiment, seed 5×10^3 H9C2 cells in 100 μL of medium per well in a 96-well plate, ensuring that the edge wells are filled with sterile PBS to minimize evaporation. After 24 h, discard the transfection system and replace it with a sugar-free, serum-free DMEM (dulbecco's modified eagle medium). Place the culture plates in a trigas incubator (Cat No: MCO-5M) were obtained from PHC Health Medical Devices (Shanghai, China) with the gas conditions set to 94.5% N_2, 0.5% O_2, and 5% CO_2. Cultivate the cells for three duration periods: 14, 16, and 18 h. For the control group, wash the cells twice with PBS, then add 100 μL of high-glucose serum-containing medium to each well. Incubate the control group in a 37 °C CO_2 incubator for the same time intervals as the model group. Finally, measure the absorbance of each well at 450 nm.

2.5. The Administered Concentration Is Determined Using CCK-8. For the experiment, seed 5×10^3 H9C2 cells in 100 μL of medium per well in a 96-well plate, ensuring that the edge wells are filled with sterile PBS to minimize evaporation. Prepare a control group alongside CAT treatment groups at concentrations of 56 μM, 28 μM, and 14 μM. After a 24-h incubation, carefully remove the old culture medium and apply the designated drug treatment to each group. Following another 24-h incubation, discard the medium containing the drugs and add 10% CCK-8 detection solution to each well. Incubate for 1 h, then measure the absorbance of each well at 450 nm.

2.6. Levels of Reactive Oxygen Species (ROS) Detection. The experiment was set up with control, OGD/R, and CAT (28uM) groups, and the OGD/R and CAT groups were subjected to OGD/R. At the end of modeling, the original medium was discarded, and the OGD/R and CAT groups were given a complete medium containing 10% fetal bovine serum with or without the drug, respectively. After 24 h of incubation, the old drug-containing medium was discarded. For each specimen, three replicate wells were prepared in accordance with the guidelines provided in the ROS Detection Kit. The level of ROS in each group's cells was measured.

2.7. Cell Transfection. The H9C2 cells were categorized into several groups: the normal group, the miR-126 NC + OGD/R group, the OGD/R + miR-126 NC + CAT group, the OGD/R + miR-126 inhibitor group, and the OGD/R + miR-126 inhibitor + CAT group. Once the H9C2 cells reached the logarithmic growth phase and attained a confluency of 70%, they were transfected using a transfection reagent at a final concentration of 20 nM (Table 1).

2.8. Determination of Lactate Dehydrogenase (LDH) Content. Select healthy H9C2 cells and seed them into a 96-well plate at a density of 5×10^3 cells per well (100 μL). After allowing the cells to adhere for 24 h, proceed to transfect, treat, model, and culture them according to the specific experimental

Table 1. Sequence of miR-126 Inhibitor

primer name	primer sequences
miR-126a-3p	CGCAUUAUUACUCACGGUACGA

conditions for each group. After the experiment, transfer 50 μL of supernatant from each group to a new 96-well plate. Adhere to the instructions provided with the LDH assay kit and measure the absorbance values at a wavelength of 490 nm.

2.9. RNA Extraction and RT-PCR. The expression of miR-126 was initially measured in three groups: the control group, the OGD/R group, and the CAT group, following the modeling process. Subsequently, we evaluated the effectiveness of miR-126 knockdown after cell transfection, with the primer sequences provided in Table 2. The effect of CAT on gene expression in the pathway via miR-126 was assessed following Zhang et al.[27] The H9c2 cells were then categorized into five groups: the control group, the OGD/R + miR-126 NC group, the OGD/R + miR-126 NC + CAT group, the OGD/R + miR-126 inhibitor group, and the OGD/R + miR-126 inhibitor + CAT group. After transfection, modeling, and treatment, each group consisted of three replicates. RNA isolation was conducted using the FastPure Cell/Tissue Total RNA Isolation Kit. The integrity and concentration of the RNA samples were assessed using a micro nucleic acid protein detector, with the primer sequences provided in Table 3.

2.10. Western Blot Analysis. The effect of CAT on protein expression in the pathway via miR-126 was assessed following Zhang et al.[27] Initiate by seeding H9C2 cells at a density of 2×10^5 cells per well in a 6-well plate. After allowing them to incubate for 24 h, proceed with transfection, modeling, and drug treatment as previously outlined. To extract total proteins from the H9C2 cells, use RIPA lysis buffer and quantify the protein concentration using the BCA method. Next, perform a 10% SDS-PAGE gel electrophoresis followed by membrane transfer. Block the membrane with 5% BSA for 1 h, then incubate it with primary antibodies targeting TWEAK (1:1000), FN14 (1:1000), NF-κB-p65 (1:1000), NF-κB−P−P65 (1:1000), NLRP3 (1:1000), TNF-α (1:2000), and β-actin (1:1000). Gently shake the membrane overnight at 4 °C. After incubation, wash the membrane three times with 1× TBST, then add the secondary antibody (1:8000). Proceed with three additional washes using 1× TBST. Detect chemiluminescence using an enhanced chemiluminescence method, and utilize the AzureC300 chemiluminescence imaging system to capture the protein band intensities. Finally, analyze these intensities using ImageJ software version 1.8.0.

2.11. MD and MDS. *2.11.1. MD.* The protein structure files for TWEAK, FN14, TNF-α, NLRP3, and NF-κB were sourced from Alpha Fold.[28] The three-dimensional (3D) structure of CAT was obtained from the PubChem database.[29,30] Following the methodology proposed by Liu,[31] we utilized AutoDock Tools to prepare the 3D structures of the key components as well as the crystal structures of the core proteins. We then carried out MD of the ligands and receptors using AutoDock Vina.[32] Finally, visual analysis was performed using PyMOL and Discovery Studio.

2.11.2. MDS. After docking, MDS was conducted using Gromacs 2022.2 software, along with the AMBER ff14SB force field and the TIP3P water model, to evaluate the stability of conformations exhibiting the lowest binding energy.[33] The complex was positioned within an octahedral box, ensuring a minimum distance of 1.2 nm between the protein atoms and the box edges. Energy minimization was executed using the steepest descent method until the energy converged to 1,000 kJ/mol/nm. Subsequently, a variety of scripts integrated within GROMACS were employed to analyze the simulation trajectories.

2.12. Combined with Free Energy Calculations. We utilized gmx_MMPBSA to analyze the final 20 ns of each trajectory in our calculations. This approach enabled us to assess the binding free energy between the ligand and receptor, along with the contribution of each residue to the overall binding energy.[33] The tool employs the Molecular Mechanics-Poisson−Boltzmann Surface Area (MM/GBSA) method to compute the binding free energy of complex structures.

2.13. ADMET Characteristic Prediction. The ADMET analysis can potentially minimize research costs to the maximum extent.[34] Based on the MD results, we uploaded the normalized ligand SMILES to the pharmacokinetics using graph-based signatures (PKCSM) server to study ADMET properties.[35]

2.14. Statistical Analysis. Statistical analysis was performed using Prism 9.5 software (GraphPad, San Diego, CA). When necessary, group comparisons were analyzed using *t* tests or Mann−Whitney U tests. A p-value <0.05 was considered statistically significant (*).

3. RESULTS

3.1. CAT Reduces OGD/R-induced LDH Levels by Increasing MiR-126 Expression in H9C2 Cells. We assessed cell viability using the CCK-8 assay to determine the optimal duration of OGD and the appropriate concentration of CAT treatment. The results indicated that a 16-h OGD resulted in a cell survival rate of 59.75% (Figure 1B). Additionally, the optimal concentration of CAT (28 μM) significantly improved the survival of H9C2 cells after OGD/R ($P < 0.01$) (Figure 1C). The ROS analysis showed that the level of ROS in the cells significantly increased after OGD/R compared to the control group. Furthermore, the elevation of intracellular ROS was inhibited by CAT treatment ($P < 0.05$) (Figure 1D−E). Western blot revealed that the protein expression levels of TWEAK and Fn14 were significantly upregulated in H9C2 cells subjected to OGD/R treatment. Importantly, CAT treatment significantly suppressed these OGD/R-induced elevations. (Figure 1F−H). These findings collectively suggest that CAT exerts a protective role against

Table 2. Primer Pairs Used for RT-PCR Analysis

primer name	primer sequences
rno-mir-126a-3p-stem	GTCGTATCCAGTGCAGGGTCCGAGGTATTCGCACTGGATACGACcgcatt
rno-mir-126a-3p-F	GCCGTCGTACCGTGAGTAAT
Univ R	AGTGCAGGGTCCGAGGTATT
U6 F	GGAACGATACAGAGAAGATTAGC
U6 R	TGGAACGCTTCACGAATTTGCG

Table 3. Primer Pairs Used for RT-PCR Analysis

gene	forward (5′-3′)	reverse (5′-3′)
TNF	GGCGTGTTCATCCGTTCTC	CTTCAGCGTCTCGTGTGTTTCT
TWEAK	CAACTAGTCCGGCCTCGAAGAAG	CTGCCTGTGCTCCATCCTGTC
FN14	CACCTCCTGCCCACTTCA	CTTCTCCACCAGTCTCCTCTATG
NLRP3	CTGAAGCATCTGCTCTGCAACC	AACCAATGCGAGATCCTGACAAC
NF-κB	CGACGTATTGCTGTGCCTTC	TTGAGATCTGCCCAGGTGGTA
β-actin	GGAGATTACTGCCCTGGCTCCTA	GACTCATCGTACTCCTGCTTGCTG

OGD/R-induced inflammatory injury in H9C2 cells, potentially through modulation of the TWEAK/Fn14 signaling axis.

To ascertain whether CAT mitigates OGD-induced damage in H9C2 cells, and to understand the role of miR-126 in this process, first, we examined the levels of miR-126 in OGD/R cells treated with CAT. The result found that the levels of miR-126 in H9C2 cells significantly decreased in OGD/R cells compared to the control group. After being treated with CAT, the miR-126 levels notably increased (Figure 1I). Furthermore, To investigate the role of miR-126 in CAT-mediated alleviation of OGD damage, we employed a miR-126 inhibitor in h9c2 cells. The RT-PCR results demonstrated a significant downregulation of miR-126 in the miR-126 inhibitor treatment group compared to the control group (Figure 1J). We subsequently assessed LDH levels, which revealed that under OGD/R conditions, both the miR-126 NC group and the miR-126 inhibitor group exhibited significantly elevated LDH levels compared to the control group ($p < 0.001$). However, after treatment with CAT, the LDH levels in the OGD/R + miR-126 inhibitor + CAT group showed a significant decrease compared to the OGD/R + miR-126 inhibitor group ($p < 0.001$) (Figure 1K). Therefore, we propose that CAT attenuates LDH release in H9C2 cells by upregulating miR-126.

3.2. CAT Inhibits the Expression of TWEAK, FN14, and Related Inflammatory Factors via miR-126.

To explore whether CAT regulates the TWEAK/FN14 signaling pathway by miR-126, we assessed the expression of key proteins associated with this pathway, specifically TWEAK, FN14, TNF-α, P65, phospho-P65, and NLRP3. In H9C2 cells, mRNA levels of TWEAK, FN14, NLRP3, NF-κB, and TNF-α showed a significant increase following OGD/R. These genes exhibited a more prominent upregulation in the OGD/R + miR-126 inhibitor group compared to the OGD/R + miR-126 NC group. Conversely, treatment with CAT significantly reduced the inflammatory expression levels in the OGD/R + miR-126 inhibitor group (Figure 2A−E). We also evaluated protein levels using Western blotting, where phospho-P65 acts as an indicator of NF-κB activation. After OGD/R, the expression levels of TWEAK, FN14, P−P65/P65, NLRP3, and TNF-α significantly increased. Notably, the group treated with the miR-126 inhibitor demonstrated a substantial increase in inflammatory protein expression compared to the miR-126 negative control group. After treatment with CAT, the inflammatory levels were markedly reduced in the OGD/R + miR-126 inhibitor + CAT group compared to the OGD/R + miR-126 inhibitor group, but remained higher than in the OGD/R + miR-126 NC + CAT group (Figure 2F−K).

3.3. MD.

Our previous findings suggested that CAT protects myocardial cells from damage through the miR-126/TWEAK-FN14 signaling pathway. To further investigate whether CAT can interact with pathway protein, MD was employed. The analysis revealed that the binding energy of CAT with all five target proteins was less than or equal to −4 kcal/mol. Notably, the docking binding energy of CAT with NLRP3 registered the lowest value at −7.309 kcal/mol (Figure 3D). As shown in the figure, CAT binds tightly to the binding pockets of these core receptor proteins, maintaining stability through hydrogen bonding.

When CAT interacts with TWEAK, it forms hydrogen bonds with the amino acid residues GLY121, ARG116, and SER131 (Figure 3A). For FN14, hydrogen bonds are established with the residues GLY66, TRP42, and PHE43 (Figure 3B). For NF-κB, CAT forms a hydrogen bond with residue TYR18(Figure 3C). In the case of TNF-α, binding occurs with residues GLU186 and PRO176 (Figure 3E). In CAT/NLRP3 complex, CAT forms hydrogen bonds with residues GLU231, LYS232, THR233, ARG154, ASP153, and GLU152 (Figure 3F). Notably, NLRP3 forms more hydrogen bonds with CAT than the other proteins, which may account for its optimal binding energy.

3.4. MDS.

3.4.1. Fluctuation Values of Root-Mean-Square Deviation (RMSD), Root-Mean-Square Fluctuation (RMSF), Radius of Gyration (Rg), and Solvent Accessible Surface Area (SASA).

To explore the dynamic characteristics, stability, and functional relevance of molecules under varying conditions, we conducted MDS of CAT interaction with TWEAK and FN14 proteins. The RMSD is a critical parameter for assessing the stability and structural similarity of molecular complexes. A stable RMSD value signifies that the complex system has attained equilibrium. As depicted in the figure, the CAT-TWEAK complex reached equilibrium at 25 ns, while the RMSD of the CAT-FN14 complex stabilized at 75 ns (Figure 4A). Examining the structural flexibility of the protein following postligand binding during the MDS is crucial for comprehending residue dynamics and their interaction with the ligand. We employed the RMSF technique to assess changes in amino acid residues within the protein, which showed minimal differences in both systems (Figure 4B). The Rg is a metric of the overall compactness of the system and its stability upon ligand binding during MDS. A lower Rg value suggests a more compact structure. Both systems exhibited a slight decrease in Rg values. Additionally, we measured the SASA of the protein to investigate the compactness of its hydrophobic core (Figure 4C). A decrease in SASA indicates a diminished hydrophilic surface area of the complex, with both systems demonstrating a significant decline in SASA values (Figure 4D). These findings imply that CAT engages in intricate interactions with the protein cores, exhibiting complex and stable dynamic behavior during MDS.

3.4.2. DCCM (Dynamical Cross-Correlation Matrix).

Figures 5A and 5B depict the DCCM for various amino acid residues within the protein. The X and Y axes represent the sequence numbers of the amino acids, while the colors in the figures represents the motion correlations between different residue pairs. Blue regions signify positive correlations,

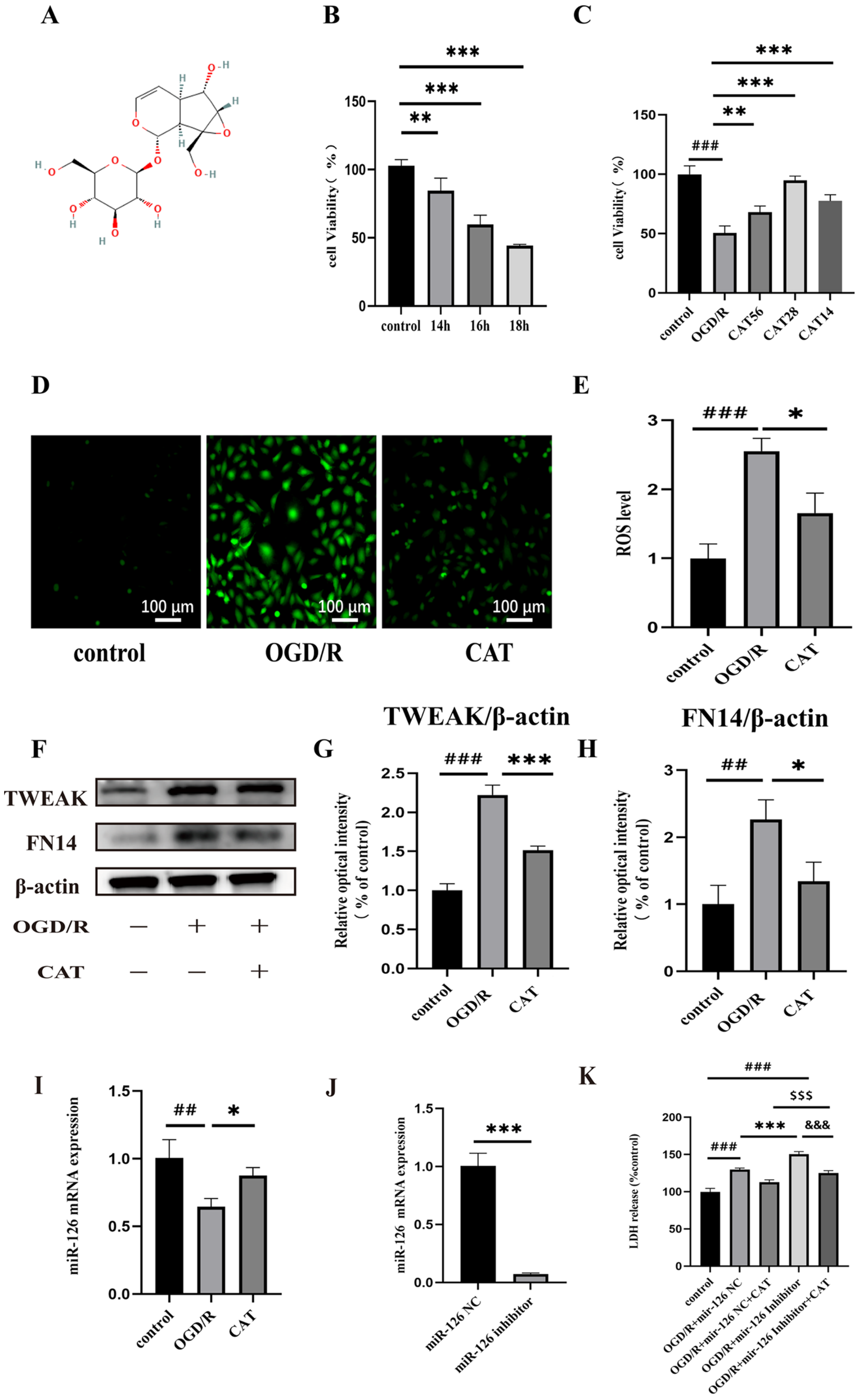

Figure 1. (A) Chemical structure of CAT. The effect of CAT on the proliferation of H9C2 cells, as assessed by CCK-8 assay for cell viability. (B) Cells were subjected to OGD/R treatment for 14 h, 16 h, and 18 h, respectively. $**p < 0.01$, $***p < 0.001$ vs control group. (C) Cells were treated with OGD/R and CAT (14, 28, 56uM) for 24 h. $\#\#\#p < 0.001$ vs control group. $**p < 0.01$, $***p < 0.001$ vs OGD/R group. (D, E) Fluorescence photographs and ROS levels. Scale bar: 100 μm. (SD ± mean, $n = 3$). $\#\#\#p < 0.001$ vs control group. $*p < 0.05$ vs OGD/R group. (F) represents images of TWEAK, and FN14 in H9C2 cells. (G, H) Quantitative expression data of TWEAK, FN14 in H9C2 cells. $\#\#p < 0.01$, $\#\#\#p < 0.001$ vs

Figure 1. continued

control group. $^{*}p < 0.5$, $^{***}p < 0.001$ vs OGD/R group. (I) RT-qPCR detection of miR-126 levels before and after CAT treatment in each group. $^{\#\#}p < 0.01$ vs control group. $^{*}p < 0.5$ vs OGD/R group. (J) RT-qPCR detection of miR-126 knockdown. $^{***}p < 0.001$ vs miR-126 NC group. (K) LDH levels were measured after CAT treatment. $^{\#\#\#}p < 0.001$ vs control group. $^{***}p < 0.001$ vs OGD/R + miR-126 NC group. $^{\$\$\$}p < 0.01$ vs OGD/R + miR-126 NC + CAT group. $^{\&\&\&}p < 0.001$ vs OGD/R + miR-126 inhibitor group.

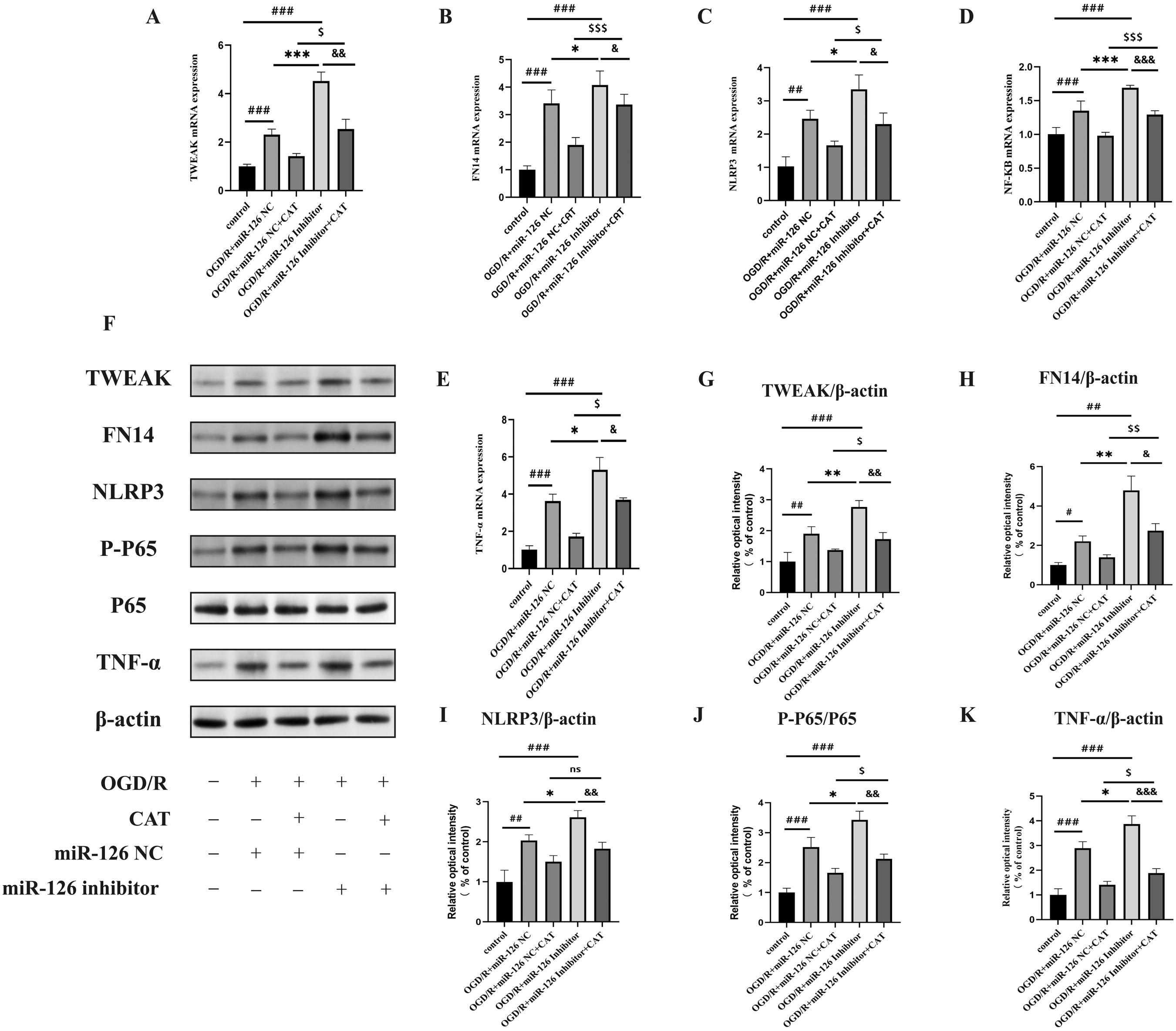

Figure 2. (A−E) Effect of CAT on the miR-126/TWEAK-FN14 signaling pathway at the gene level. Gene expression of TWEAK, FN14, NLRP3, NF-κB, and TNF-α was assessed using RT-PCR. (F) represents images of TWEAK, FN14, NLRP3, P−P65, P65, and TNF-α in H9C2 cells. (G−K) Quantitative expression data of TWEAK, FN14, NLRP3, P−P65/P65, and TNF-α in H9C2 cells. $^{\#}p < 0.05$, $^{\#\#}p < 0.01$, $^{\#\#\#}p < 0.001$ vs control group. $^{*}p < 0.05$, $^{**}p < 0.01$, $^{***}p < 0.001$ vs OGD/R + miR-126 NC group. $^{\$}p < 0.05$, $^{\$\$}p < 0.01$, $^{\$\$\$}p < 0.001$ vs OGD/R + miR-126 NC + CAT group. $^{\&}p < 0.05$, $^{\&\&}p < 0.01$, $^{\&\&\&}p < 0.001$ vs OGD/R + miR-126 inhibitor group.

indicating that the residues move together in the same direction, whereas the pink regions represent negative correlations, suggesting that the residues move in opposite directions. Notable blue (positive correlation) and pink (negative correlation) are clustered around specific residue pairs, potentially corresponding to functional domains or folding regions within the protein, such as local dynamics of alpha helices or beta sheets. Regions closer to the diagonal often represent residue pairs that are in closer proximity, typically exhibiting higher correlation. When TWEAK interacts with CAT, the protein structure demonstrates enhanced flexibility and dynamics, resulting in more pronounced positive and negative motions between residues. This suggests that the binding promotes movement in certain regions, potentially modulating protein function (Figure 5A). Conversely, when Fn14 interacts with CAT, the movements between residues become more consistent and centered, indicating that the protein structure may become more stable or compact upon

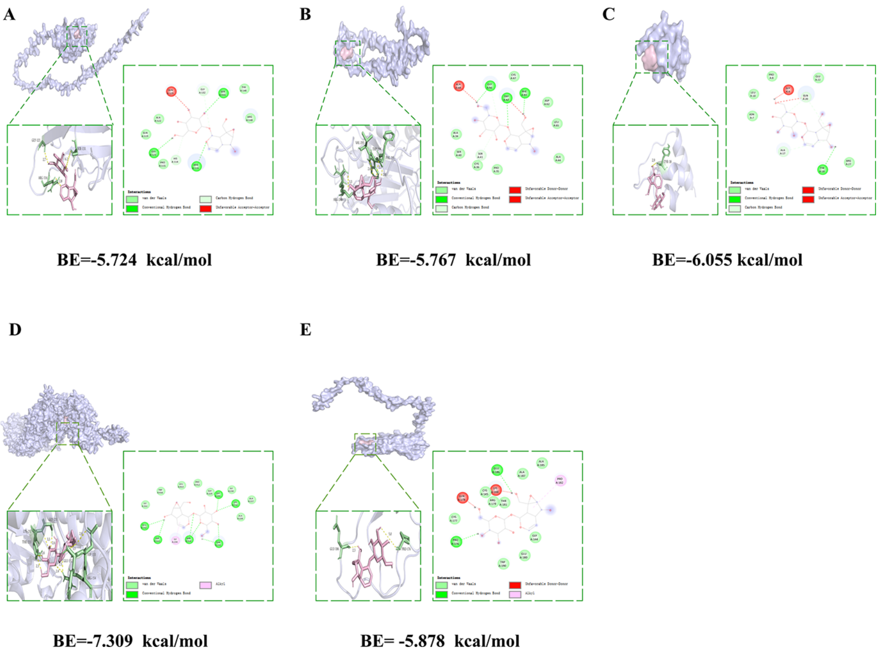

Figure 3. MD of Ca with TWEAK and FN14. (A) 3D and 2D binding diagrams of CAT with TWEAK. (B) 3D and 2D binding diagrams of CAT with FN14. (C) 3D and 2D binding diagrams of CAT with NF-κB. (D) 3D and 2D binding diagrams of CAT with NLRP3. (E) 3D and 2D binding diagrams of CAT with TNF-α.

binding. This might imply that the binding of Fn14 with CAT restricts the protein's flexibility, leading to a more ordered conformation (Figure 5B).

3.4.3. DSSP (Dictionary of Secondary Structure of Protein). In the secondary structure diagrams, we track the changes in the secondary structure of proteins over time following the binding of CAT with TWEAK and Fn14. In Figure 5, the predominance of red (β sheet) and blue (α helix), indicates that the protein maintains a stable secondary structure throughout the simulation. Specifically, in the central residue region spanning 60 to 200 aa, the continuous and uniform distribution of β sheets and α helices suggest a relatively compact and stable folding of TWEAK upon interaction with CAT. Figure 5D shows that Fn14's secondary structure is denser and more uniform, particularly in the region between residue numbers 50−100 aa, where both α helix and β sheet are prominently present. This indicates that Fn14's secondary structure becomes stable and compact after binding with CAT (Figure 5D). Upon binding to CAT, TWEAK maintains a stable secondary structure characterized by a higher proportion of β-sheets and α-helices (Figure 5C). In contrast, Fn14 exhibits more localized conformational changes at specific residues (green for bends, yellow for turns), suggesting structural bending or turn formation during the binding process (Figure 5D). This distinction may reveal their divergent interaction mechanisms with CAT: TWEAK requires preserved structural flexibility to fulfill its functional roles, while Fn14 operates through the formation of a more stable and compact conformation.

3.4.4. PCA (Principal Component Analysis). The results of PCA offer valuable insights into the parameters that govern ligand-protein interactions. Specifically, PC1 reflects the strength of ligand-protein binding, while PC2 indicates the flexibility of the ligand-protein complex. Additionally, PC3 captures changes in shape complementarity between the protein and ligand. For the PC1 clustering, the variances were 55.2% and 37.5%, whereas for PC2 clustering, they were 12.3% and 21.7%. The variances for PC3 clustering were 6.9% and 9.2%. Notably, the variance for the CAT-TWEAK system was lower at 6.9% compared to the CAT-FN14 system, suggesting fewer structural changes (Figure 6A−B). Moreover, PCA was employed to generate a two-dimensional projection that explores the dynamics of protein−ligand interactions. Motion analysis was performed using PC1 and PC2 for the two complexes. The two color-coded trajectories illustrate the conformational space traversed by TWEAK and Fn14 during the simulation, with the scattering and clustering of points indicating the degree of fluctuations for each molecule or complex. In the two-dimensional projection, stable clustering is characterized by complexes occupying smaller regions of phase space, while unstable clustering is reflected by those that span larger areas. The trajectories suggest that TWEAK undergoes more significant conformational changes than Fn14, as evidenced by its more dispersed trajectory in the 2D projection. In contrast, Fn14 appears to fluctuate within a more confined area, indicating a more stable structure throughout the simulation (Figure 6C).

3.4.5. FEL (Free Energy Landscape). FEL analysis is employed to gain conformational changes of a system and to compute Gibbs free energy using RMSD and Rg values. The FEL plot displays RMSD, Rg, and Gibbs free energy on the X, Y, and Z axes, respectively. Figure 6D,E illustrates the distribution of free energy across various molecular conformations. Regions characterized by low RMSD and a low gyration radius correspond to more compact conformations, while areas with high RMSD and a high gyration radius reflect more extensive or larger-scale conformational shifts. The color gradient in these figures enhances our understanding of the relative stability of the conformations. Orange regions indicate lower free energy states, often signifying stable configurations

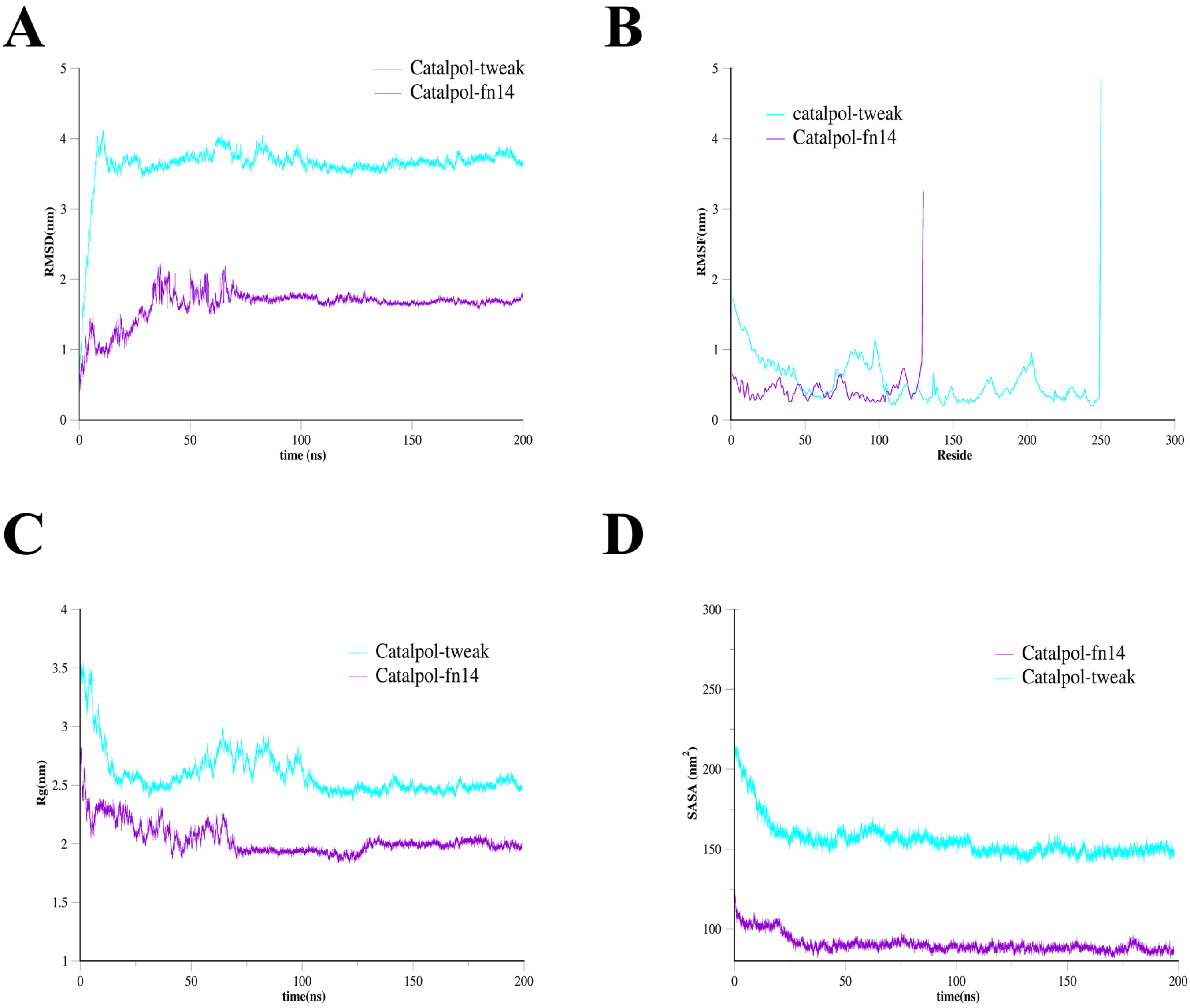

Figure 4. (A–D) CAT with TWEAK, FN14 complex MDS. (A) RMSD. (B) RMSF. (C) Rg. (D) SASA.

or energy minima, such as the equilibrium state of the molecular system. In contrast, orange to dark blue represents an increase in free energy, typically corresponding to transition states or higher-energy unstable conformations. The CAT-TWEAK complex achieved the lowest free energy (LFE) at 2.5 nm RMSD and 2.5 nm Rg, while the CAT-FN14 complex attained its LFE at 1.6 nm RMSD and 1.95 nm Rg. The complex formed with FN14 exhibited a narrower and deeper energy well, indicative of higher specificity and stable binding conformation, this structural feature suggests that the complex formed with FN14 likely operates within a restricted range of conformational changes, enhancing its functional stability. In contrast, the complex with TWEAK exhibited a broader energy well, implying that CAT adopts a wider spectrum of stable conformations when interacting with this ligand.

3.5. Combining Free Energy Calculations and Hydrogen Bond Analysis.

Integrating free energy calculations provides a quantitative foundation for understanding molecular interactions, which is crucial in guiding drug design and molecular engineering. In this study, the binding free energies of two complexes were determined using the MM-GBSA method. Throughout the MDS, the binding energy of CAT with TWEAK was measured at −13.06 ± 4.01 kcal/mol, while the binding energy of CAT with FN14 was −17.69 ± 3.99 kcal/mol (Figure 7B,E, Table 4). Fluctuations in the number of hydrogen bonds observed during the simulation indicate conformational changes and structural rearrangements. Notably, the CAT-TWEAK complex demonstrates a greater number of hydrogen bonds compared to the CAT-FN14 complex, suggesting a more stable and compact binding structure (Figure 7C,F). Overall, these findings underscore the specific interactions between CAT and TWEAK, and FN14, which contribute to the formation of stable binding complexes.

3.6. ADMET Analysis Results.

To gain a comprehensive understanding of the pharmacological properties of CAT, we employed the pkCSM server to predict its ADMET (Absorption, Distribution, Metabolism, Excretion, and Toxicity) characteristics. As indicated in Table 5, CAT is characterized by low aqueous solubility and poor permeability, with an intestinal absorption rate of less than 50%. Moreover, a logBB (blood-brain barrier permeability) value of less than −1 and a logPS (predicted passive permeability) value below −3

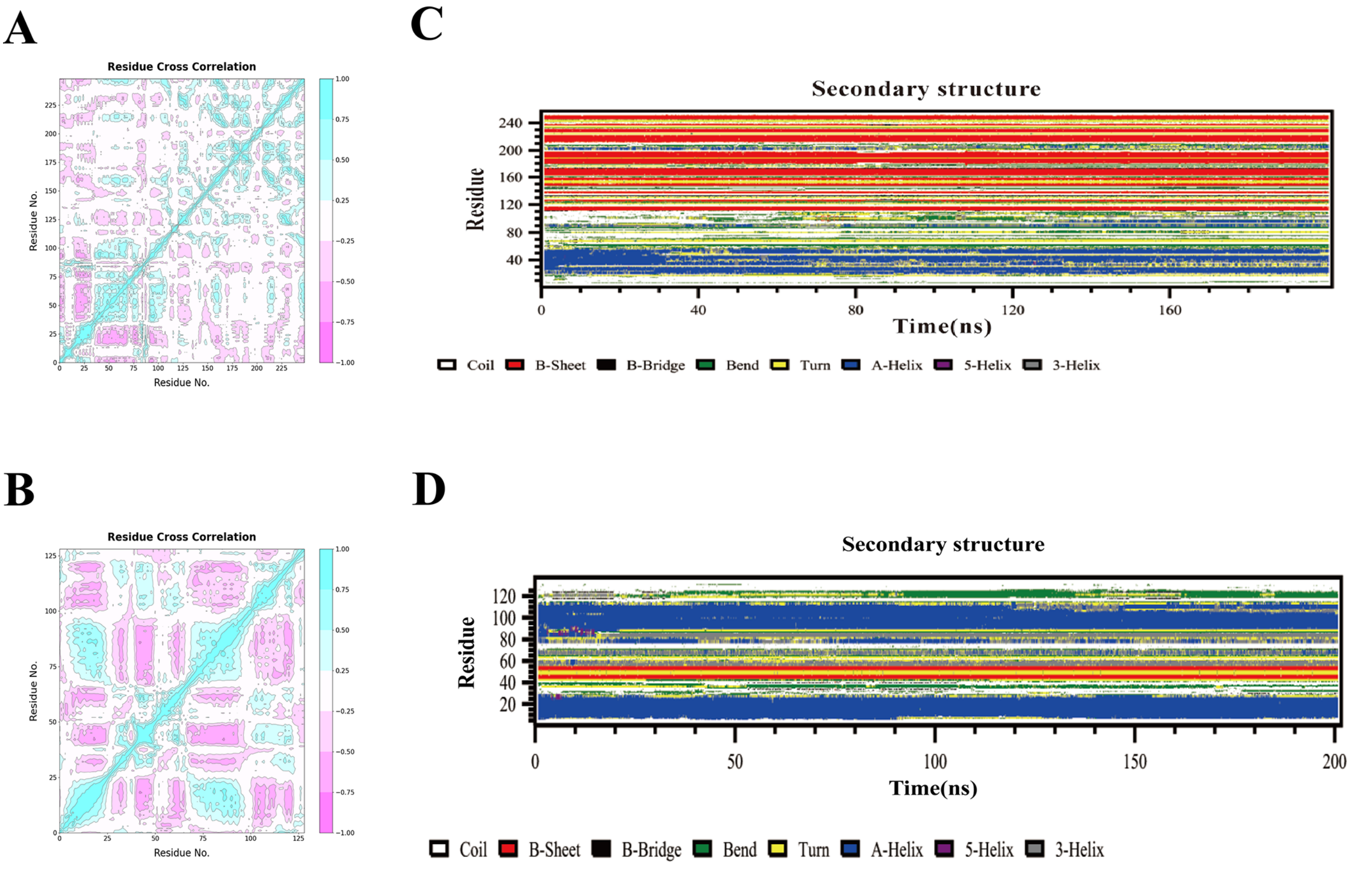

Figure 5. (A, B) Dynamic cross-correlation heatmaps: (A) CAT-TWEAK, (B) CAT-FN14, where blue regions (positive values) indicate a positive correlation in motion between residues. Pink regions (negative values) indicate a negative correlation in motion between residues. (C, D) Protein secondary structure changes: (C) CAT-TWEAK and (D) CAT-FN14. Secondary structure changes are represented by different colors as follows: coil (white), β-sheet (red), β-bridge (black), bend (green), turn (yellow), and helix (blue/purple/dark gray).

suggest that the compound has limited capacity to cross the blood-brain barrier (BBB) and enter the central nervous system (CNS), implying a potentially minimal impact on the CNS. Regarding drug metabolism, cytochrome enzymes (CYP) play a critical role; however, our analysis did not yield specific findings about this aspect.

4. DISCUSSION

Myocardial infarction is a predominant cause of death and disability attributable to cardiovascular diseases globally, particularly affecting the elderly and those with unhealthy lifestyles.[36] The investigation of natural compounds for the treatment of myocardial infarction has garnered increasing interest due to their numerous biological activities, including antioxidant, anti-inflammatory, antithrombotic, and blood circulation-enhancing properties.[37,38] For instance, quercetin and apigenin are known for their antioxidant and anti-inflammatory effects, which can protect myocardial cells from ischemia-reperfusion injury.[39−41] Studies have also indicated that resveratrol and epigallocatechin gallate (EGCG), a component of green tea, can mitigate myocardial cell damage and enhance cardiac function.[42,43] Furthermore, berberine can alleviate mitochondrial damage and reduce the risk of myocardial infarction.[44,45]

In recent years, CAT has garnered attention for its potential in the treatment of inflammatory diseases. Studies suggest that it can inhibit the activation of the NF-κB signaling pathway.[46,47] By blocking IκB degradation and nuclear translocation, CAT significantly reduces the release of inflammatory factors, helping to alleviate the inflammatory mediators, thereby mitigating.[10,48] During MI/R, the inflammatory response can exacerbate damage to myocardial cells.[49−51] Studies have shown that CAT can diminish postreperfusion inflammation by inhibiting the expression of pro-inflammatory cytokines, such as TNF-α and IL-1β, and also reducing leukocyte infiltration within the myocardium.[52,53]

miR-126 is a microRNA that plays a vital role in various biological processes and diseases, particularly within the cardiovascular system.[21,54,55] It is especially significant in conditions such as atherosclerosis, myocardial infarction, and ischemic diseases. By targeting and down-regulating molecules linked to cell apoptosis, miR-126 facilitates the survival of myocardial cells.[56] In this study, we initially established an OGD/R model to explore the anti-inflammatory effects of CAT. After administration, CAT significantly inhibited intracellular ROS production and significantly increased intracellular miR-126 levels. Subsequently, we performed cell transfection, and the RT-PCR data revealed a noteworthy reduction in intracellular miR-126 levels. Additionally, CAT administration reduced the LDH level in the miR-126 inhibitor group. These results suggest that CAT may alleviate inflammation by enhancing intracellular miR-126 levels.

TWEAK, a member of the tumor necrosis factor (TNF) superfamily, exerts its biological effects by binding to the Fn14 receptor.[57] Normally, Fn14 is expressed at low levels in the myocardium, but its expression significantly increases during

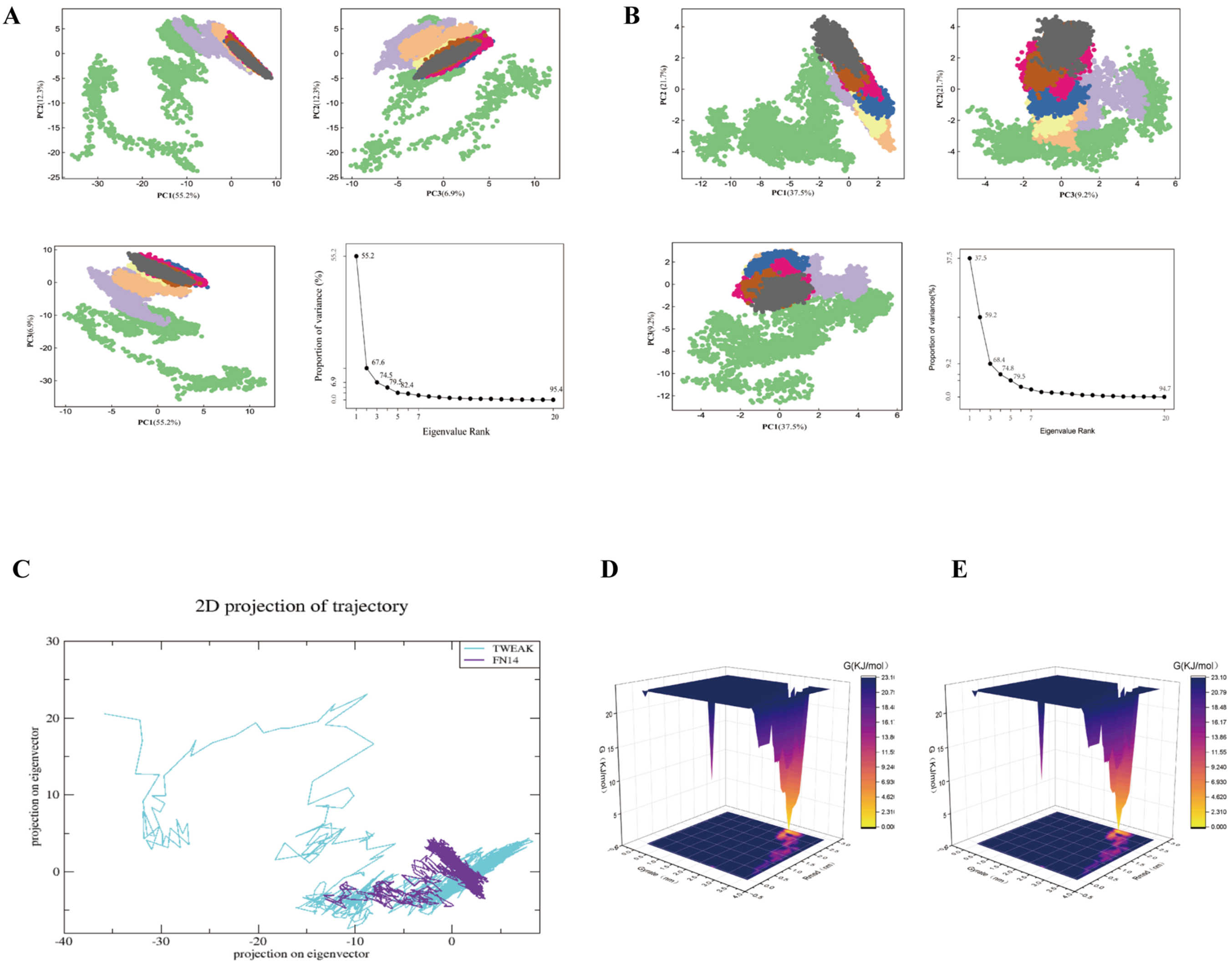

Figure 6. (A–C) Graphical representation of the PCA analysis of the complexes. (A) CAT-TWEAK. (B) CAT-FN14. (C) 2D projection of the trajectory on the eigenvectors of the principal component analysis of the dynamics of protein–ligand interactions for CAT with TWEAK and FN14. (D, E) Graphical representation of the Gibbs free energy landscape obtained from dynamic simulation studies. (D) FEL of the CAT-TWEAK complex. (E) FEL of the CAT-FN14 complex.

conditions such as MI/R injury, and myocardial infarction, particularly in damaged myocardial cells, endothelial cells, and cardiac fibroblasts.[58,59] Experimental results show that after OGD/R, the levels of TWEAK and Fn14 in both the miR-126NC group and miR-126 inhibitor group were markedly elevated. However, CAT treatment effectively inhibited the up-regulation of TWEAK and Fn14 expression following OGD/R. We propose that CAT inhibits the expression and activation of the TWEAK and Fn14 signaling pathways by up-regulating miR-126.

The TWEAK/Fn14 pathway is intricately linked to the NLRP3 inflammasome and the NF-κB pathway, both of which play pivotal roles in inflammatory responses, tissue damage, and fibrosis. TWEAK, through its receptor Fn14, activates multiple signaling pathways that provoke pro-inflammatory responses and tissue remodeling. NLRP3 and NF-κB serve as crucial regulators of these inflammatory processes. The TWEAK/Fn14 signaling pathway can directly activate NF-κB, which is vital for facilitating inflammatory responses and regulating immune functions.[23,60] NF-κB is a key transcription factor that modulates the expression of various genes.[61] Our data suggest that CAT may mitigate the inflammatory response following OGD/R by upregulating miR-126 and inhibiting the phosphorylation of NF-κB. NF-κB is recognized as a transcriptional regulator of the NLRP3 gene, and TWEAK enhances the expression of NLRP3 and its downstream targets by activating the NF-κB pathway.[62] In this study, we discovered that the knockdown of miR-126 resulted in the activation of the TWEAK/Fn14 pathway, thereby triggering the downstream NLRP3 inflammasome. This activation was effectively reversed through treatment with CAT. Furthermore, TNF-α, a strong pro-inflammatory cytokine, can induce both cell apoptosis and necrosis. Our research indicates that CAT treatment significantly inhibits the effects of TNF-α.

This study includes MD of CAT with TWEAK, FN14, NF-κB, NLRP3, and TNF-α to explore its pharmacological targets. Notably, CAT, recognized for its anti-inflammatory properties, exhibits a strong affinity for these five targets, underscoring its significant role in the regulation of inflammation.

Additionally, we employed MDS, a powerful method for assessing the stability of protein–ligand complexes and visualizing structural dynamics throughout the simulation.[63,64]

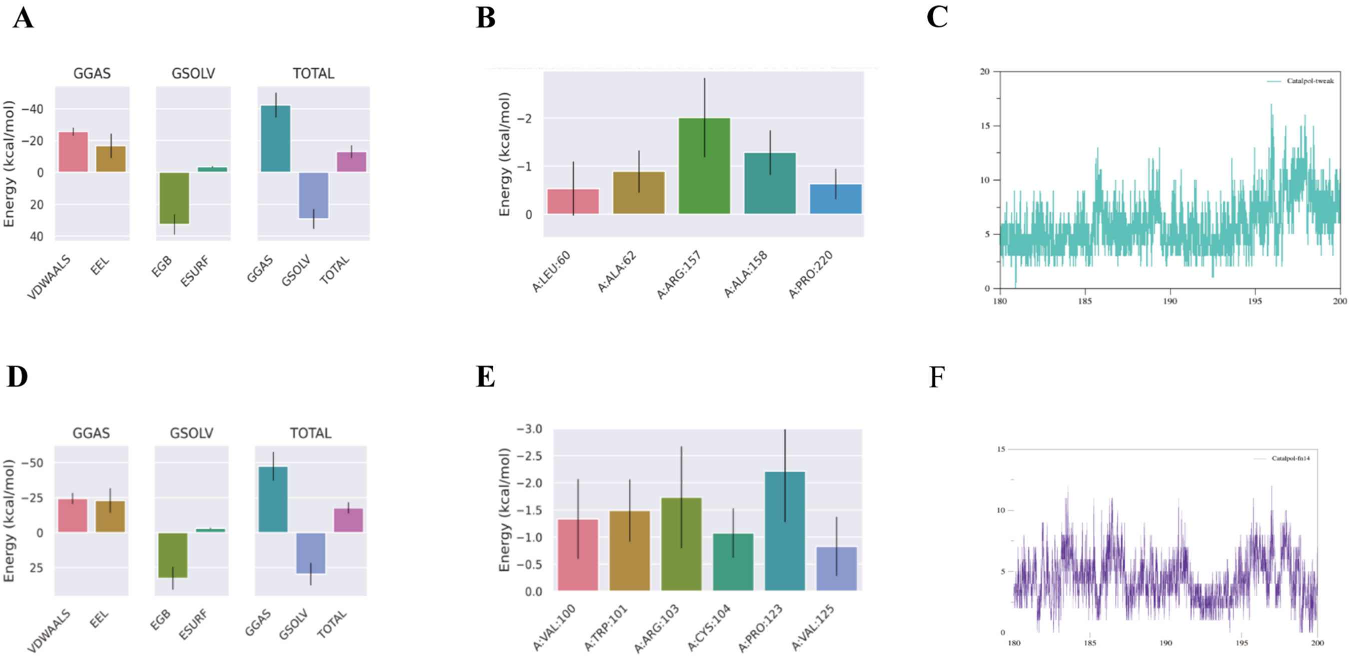

Figure 7. Combined free energy analysis and hydrogen bond analysis based on the average structure of the last 20 ns. (A) Energy decomposition plot of CAT-TWEAK. (B) Amino acid decomposition plot of CAT-TWEAK. (C) Number of hydrogen bonds in CAT-TWEAK. (D) Energy decomposition plot of CAT-FN14. (E) Amino acid decomposition plot of CAT-FN14. (F) Number of hydrogen bonds in CAT-FN14. Energy amino acid decomposition was calculated using a TDC-based method. VDWAALS, van der Waals energy; EEL, electrostatic solvation energy; EGB, polar solvation energy; ESURF, nonpolar solvation energy; GGAS, total gas-phase free energy; GSOLV, total solvation free energy; TOTAL, GSOLV + GGAS.

Table 4. MM/GBS Analysis of TWEAK&FN14 with CAT[a]

bioactive	VAWAALS	EEL	EGB	ESURF	GGAS	GSOLV	TOTAL
TWEAK	−25.58 ± 2.49	−16.67 ± 7.56	32.61 ± 6.31	−3.42 ± 0.32	−42.25 ± 7.8	29.19 ± 6.17	−13.06 ± 4.01
FN14	−24.41 ± 3.97	−22.94 ± 8.75	32.65 ± 8.14	−2.99 ± 0.38	−47.35 ± 10.25	29.66 ± 7.95	−17.69 ± 3.99

[a] Each parameter is expressed in kcal/mol, and the data are presented as mean ± SD.

This approach enabled us to evaluate CAT's binding stability to the TWEAK and FN14 pockets throughout 200 ns. The obtained RMSD, Rg, SASA, and RMSF data indicate that each complex system demonstrates high stability in a human-like environment. Throughout the MDS, the patterns of hydrogen bonds and hydrophobic interactions closely correlate with the MD results, suggesting significant flexibility between the ligands and their corresponding receptors. Furthermore, calculations of binding free energy indicate a strong affinity between the ligands and receptors in each complex. Dynamic cross-correlation matrix graphs reveal the movement correlations of various residues in the protein under two conditions. Analysis of the protein's secondary structure indicates that TWEAK requires the retention of structural flexibility to exert its functional roles, while Fn14 operates through the formation of a more stable and compact conformation. The results of PCA provide valuable insights into the parameters governing ligand-protein interactions. The results from the energy landscape map, derived from the combined analysis of RMSD and the radius of gyration, illustrate the energy transition process from tightly folded to unfolded states within the system. Furthermore, the predicted pharmacokinetic properties of CAT are promising. In conclusion, the insights gained from MDS and binding free energy calculations mutually reinforce the pharmacological characteristics of CAT.MDS results indicate that CAT exhibits strong binding affinity with both TWEAK and FN14, along with good stability. Our previous experiments demonstrated that CAT administration significantly upregulates miR-126 levels. Therefore, we propose that CAT can enhance miR-126 expression, thereby suppressing the expression of inflammatory genes in the TWEAK/FN14 pathway. Additionally, CAT may directly bind to TWEAK and FN14, leading to reduced expression of these genes.

This study has demonstrated that CAT exerts beneficial effects on inflammation following MI/R and regulates the miR-126/TWEAK-FN14 pathway. However, given the intricate nature of the pathological processes involved in MI/R injury, our study serves as a preliminary investigation. Future Further studies are imperative to uncover the full spectrum of underlying mechanisms. Regrettably, time constraints and other practical factors have prevented us from including a more extensive in vivo mechanistic study in this paper. Nevertheless, we are currently engaged in a comprehensive in vivo study to further investigate the protective effects of CAT on MI/R injury in the heart.

5. CONCLUSIONS

In summary, CAT enhances miR-126 expression, thereby the miR-126/TWEAK-FN14 pathway. This activation reduces inflammation and lowers LDH levels in H9C2 cells following

Table 5. Prediction of ADMET Properties of CAT

property	model name	predicted value	unit
absorption	water solubility	−2.176	numeric (logmol/L)
	Caco-2 permeability	0.397	numeric (logPappin10−6 cm/s)
	intestinal absorption (human)	31.129	numeric (% absorbed)
	P-glycoprotein substrate	yes	categorical (yes/no)
	P-glycoprotein inhibitor	no	categorical (yes/no)
	P-glycoprotein inhibitor	no	categorical (yes/no)
	VDss (human)	0.002	numeric (logL/kg)
distribution	fraction unbound (human)	0.74	numeric (Fu)
	BBB permeability	−1.126	numeric (logBB)
	CNS permeability	−4.275	numeric (logPS)
	CYP2D6 substrate	no	categorical (yes/no)
metabolism	CYP3A4 substrate	no	categorical (yes/no)
	CYP1A2 inhibitor	no	categorical (yes/no)
	CYP2C19 inhibitor	no	categorical (yes/no)
	CYP2C9 inhibitor	no	categorical (yes/no)
	CYP2D6 inhibitor	no	categorical (yes/no)
	CYP3A4 inhibitor	no	categorical (yes/no)
	total clearance	1.238	numeric (logmL/min/kg)
excretion	renal OCT2 substrate	no	categorical (yes/no)
	AMES toxicity	no	categorical (yes/no)
toxicity	max. tolerated dose (human)	0.878	numeric (logmg/kg/day)
	hERGI inhibitor	no	categorical (yes/no)
	hERGII inhibitor	no	categorical (yes/no)
	hepatotoxicity	no	categorical (yes/no)

OGD/R. Therefore, CAT shows considerable potential as a therapeutic agent for the treatment of MI/R.

AUTHOR INFORMATION

Corresponding Authors

Haitong Wan − *College of Basic Medical Sciences, Zhejiang Chinese Medical University, Zhejiang, Hangzhou 310053, China; College of Chinese Medical Sciences, Henan University of Chinese Medicine, Zhengzhou, Henan 450046, China;* orcid.org/0009-0005-0776-0269; Email: whtong@126.com

Jiehong Yang − *College of Basic Medical Sciences, Zhejiang Chinese Medical University, Zhejiang, Hangzhou 310053, China;* Email: yjhong@zcmu.edu.cn

Authors

Ting Wang − *College of Basic Medical Sciences, Zhejiang Chinese Medical University, Zhejiang, Hangzhou 310053, China;* orcid.org/0009-0007-3650-973X

Chongyu Shao − *College of Basic Medical Sciences, Zhejiang Chinese Medical University, Zhejiang, Hangzhou 310053, China*

Huiyan An − *College of Life Science, Zhejiang Chinese Medical University, Zhejiang, Hangzhou 310053, China;* orcid.org/0009-0009-0046-6410

Guanfeng Xu − *College of Basic Medical Sciences, Zhejiang Chinese Medical University, Zhejiang, Hangzhou 310053, China*

Complete contact information is available at: https://pubs.acs.org/10.1021/acsomega.4c11357

Author Contributions

[†]T.W. and C.S. contributed equally to this work and share first authorship.

Notes

The authors declare no competing financial interest.

ACKNOWLEDGMENTS

This work was supported by the National Natural Science Foundation of China (no. 82330120), the Natural Science Foundation of Zhejiang Province (no. LZ23H270002), and the Key Laboratory of TCM Encephalopathy of Zhejiang Province (no. 2020E10012). Thank you for the support of the above funds and institutions, and we thank pixabay for providing image materials.

REFERENCES

(1) Dada, A.; da Silva, R. d. C. V; Zanovello, M.; Moser, J. C.; Orengo, S. L.; Cavichiolo, M. O.; Bidinha, E. R.; Boeing, T.; Cechinel-Filho, V.; de Souza, P. Comparative Analysis of the Protective Effect of Naringenin on Cardiovascular Parameters of Normotensive and Hypertensive Rats Subjected to the Myocardial Infarction Model. *Pharmaceuticals* **2024**, *17* (10), 1324.

(2) Wang, Y.; Tian, F.; Qian, Z.; Ran, S.; Zhang, J.; Wang, C.; Chen, L.; Zheng, D.; Vaughn, M.; Tabet, M.; Lin, H. Healthy Lifestyle, Metabolic Signature, and Risk of Cardiovascular Diseases: A Population-Based Study. *Nutrients* **2024**, *16* (20), 3553.

(3) Guo, Z.; Tian, Y.; Liu, N.; Chen, Y.; Chen, X.; Yuan, G.; Chang, A.; Chang, X.; Wu, J.; Zhou, H. Mitochondrial Stress as a Central Player in the Pathogenesis of Hypoxia-Related Myocardial Dysfunction: New Insights. *International Journal of Medical Sciences* **2024**, *21* (13), 2502.

(4) Lu, L.; Liu, M.; Sun, R.; Zheng, Y.; Zhang, P. Myocardial infarction: symptoms and treatments. *Cell Biochem. Biophys.* **2015**, *72*, 865−867.

(5) Koracevic, G.; Micic, S.; Stojanovic, M.; Tomasevic, M.; Kostic, T.; Velickovic Radovanovic, R.; Lovic, D.; Djordjevic, D.; Randjelovic, M.; Koracevic, M.; Ristic, Z. Beta blocker rebound phenomenon is important, but we do not know its definition, incidence or optimal prevention strategies. *Hypertension Res.* **2020**, *43* (7), 591−596.

(6) Zhang, L.; Bao, Y.; Tao, S.; Zhao, Y.; Liu, M. The association between cardiovascular drugs and depression/anxiety in patients with cardiovascular disease: a meta-analysis. *Pharmacol. Res.* **2022**, *175*, No. 106024.

(7) Chen, Y.; Liu, Q.; Meng, X.; Zhao, L.; Zheng, X.; Feng, W. Catalpol ameliorates fructose-induced renal inflammation by inhibiting TLR4/MyD88 signaling and uric acid reabsorption. *Eur. J. Pharmacol.* **2024**, *967*, No. 176356.

(8) Nie, W.; Zhu, H.; Sun, X.; Zhou, J.; Xu, H.; Yu, Z.; Lu, M.; Jiang, B.; Zhou, L.; Zhou, X. Catalpol attenuates hepatic glucose metabolism disorder and oxidative stress in triptolide-induced liver injury by regulating the SIRT1/HIF-1α pathway. *International Journal of Biological Sciences* **2024**, *20* (10), 4077.

(9) Liu, K.; Yao, X.; Gao, J.; Wang, J.; Qi, J. A study on the mechanism of Beclin-1 m6A modification mediated by catalpol in protection against neuronal injury and autophagy following cerebral ischemia. *Mol. Med.* **2024**, *30* (1), 65.

(10) Pang, Y.; Zhao, L.; Ji, X.; Guo, K.; Yin, X. Analyses of transcriptomics upon IL-1β-stimulated mouse chondrocytes and the protective effect of catalpol through the NOD2/NF-κB/MAPK signaling pathway. *Molecules* **2023**, *28* (4), 1606.

(11) Soták, M.; Clark, M.; Suur, B. E.; Börgeson, E. Inflammation and resolution in obesity. *Nat. Rev. Endocrinol.* **2024**, 45−61.

(12) Yu, H.; Li, Q.; Zhu, H.; Liu, C.; Chen, W.; Sun, L. Mesenchymal stem cells attenuate systemic lupus erythematosus by

inhibiting NLRP3 inflammasome activation through Pim-1 kinase. *International Immunopharmacology* **2024**, *126*, No. 111256.

(13) Huang, B.; Zhang, J.; Tian, H.; Ren, S.; Chen, K.; Feng, J.; Fan, S.; Tuo, Y.; Wang, X.; Yu, L.; Ma, C.; Peng, Q.; Chen, X.; He, R.; Li, G. Metformin modulates the TXNIP-NLRP3-GSDMD pathway to improve diabetic bladder dysfunction. *Sci. Rep.* **2024**, *14* (1), 1−10.

(14) Cai, G.; Song, X.; Luo, H.; Dai, G.; Zhang, H.; Jiang, D.; Lei, X.; Chen, H.; Zhang, L. NLRP3 blockade by MCC950 suppressed osteoclastogenesis via NF-κB/c-Fos/NFATc1 signal pathway and alleviated bone loss in diabetes mellitus. *Mol. Cell. Endocrinol.* **2024**, *594*, No. 112382.

(15) He, X.; Wu, T.; He, H.; Chen, L.; Han, K.; Zheng, J.; Zhang, Z.; Yuan, S.; Wang, Y.; Zhang, Y.; Zhang, X.; Xie, C. Study of kaempferol in the treatment of rheumatoid arthritis through modulation of the NLRP3/CASP1/GSDMD axis and T-cell activation: Based on network pharmacology, single-cell analysis, and experimental validation. *Int. Immunopharmacol.* **2024**, *143*, No. 113357.

(16) Wang, Y. l.; Wu, H. r.; Zhang, S. s.; Xiao, H. l.; Yu, J.; Ma, Y. y.; Zhang, Y. d.; Liu, Q. Catalpol ameliorates depressive-like behaviors in CUMS mice via oxidative stress-mediated NLRP3 inflammasome and neuroinflammation. *Transl. Psychiatry* **2021**, *11* (1), 353.

(17) Tang, S.-t.; Wang, F.; Shao, M.; Wang, Y.; Zhu, H.-q. MicroRNA-126 suppresses inflammation in endothelial cells under hyperglycemic condition by targeting HMGB1. *Vascular pharmacology* **2017**, *88*, 48−55.

(18) Wang, Y. E.; Chen, J.; Yang, H.; He, J.; Varier, K. M.; Chen, Y.; Wu, X.; Guo, Q.; Liang, Y.; Shen, X.; Wei, M.; Li, W.; Tao, L. Polysialic acid driving cardiovascular targeting co-delivery 1, 8-cineole and miR-126 to synergistically alleviate lipopolysaccharide-induced acute cardiovascular injury. *Int. J. Biol. Macromol.* **2024**, *280*, No. 135970.

(19) Zhu, K.; Liu, C.; Guo, X.; Zhang, X.; Xie, J.; Xie, S.; Qi, Q.; Yang, B. Exosomal miR-126−3p: Potential protection against vascular damage by regulating the SLC7A5/mTOR Signalling pathway in human umbilical vein endothelial cells. *Scand. J. Immunol.* **2024**, *99* (4), No. e13354.

(20) Wei, X.; Han, M.; Yang, F.; Wei, G.; Liang, Z.; Yao, H.; Ji, C.; Xie, R.; Gong, C.; Tian, Y. Biological significance of miR-126 expression in atrial fibrillation and heart failure. *Braz. J. Med. Biol. Res.* **2015**, *48*, 983−989.

(21) Chen, J.; Cui, C.; Yang, X.; Xu, J.; Venkat, P.; Zacharek, A.; Yu, P.; Chopp, M. MiR-126 Affects Brain-Heart Interaction after Cerebral Ischemic Stroke. *Transl. Stroke Res.* **2017**, *8* (4), 374−385.

(22) Yang, M.; Ge, H.; Ji, S.; Li, Y.; Xu, L.; Bi, Z.; Bu, B. TWEAK and Fn14 are overexpressed in immune-mediated necrotizing myopathy: implications for muscle damage and repair. *Rheumatology* **2023**, *62* (11), 3732−3741.

(23) Yang, B.; Yan, P.; Gong, H.; Zuo, L.; Li, B. TWEAK protects cardiomyocyte against apoptosis in a PI3K/AKT pathway dependent manner. *American Journal of Translational Research* **2016**, *8* (9), 3848−3860.

(24) Santamaría, M. H.; Ríos, L. D.; Corral, R. S. Chronic Trypanosoma cruzi infection activates the TWEAK/Fn14 axis in cardiac myocytes and fibroblasts driving structural and functional changes that affect the heart. *Experimental Parasitology* **2023**, *248*, No. 108491.

(25) Unudurthi, S. D.; Nassal, D. M.; Patel, N. J.; Thomas, E.; Yu, J.; Pierson, C. G.; Bansal, S. S.; Mohler, P. J.; Hund, T. J. Fibroblast growth factor-inducible 14 mediates macrophage infiltration in heart to promote pressure overload-induced cardiac dysfunction. *Life sciences* **2020**, *247*, No. 117440.

(26) Yin, A.; Fu, Y.; Wang, T.; Li, H.; Wang, X.; Ye, X.; Dong, P.; Yao, W. Fu-Zheng-Li-Fei Recipe (FZLFR) in the treatment of cancer cachexia: Exploration of the efficacy and molecular mechanism based on chemical characterization, experimental research and network pharmacology. *Journal of Ethnopharmacology* **2025**, *337*, No. 118929.

(27) Zhang, G.; Sun, C.; Zhou, G.; Zhang, Q. Luteolin protects mouse hippocampal neuronal cells against isoflurane-induced neurotoxicity through miR-214/PTEN/Akt pathway. *NeuroToxicology* **2024**, *103*, 310−319.

(28) Scardino, V.; Di Filippo, J. I.; Cavasotto, C. N. How good are AlphaFold models for docking-based virtual screening? *Iscience* **2023**, *26* (1), No. 105920.

(29) Kim, S. Getting the most out of PubChem for virtual screening. *Expert opinion on drug discovery* **2016**, *11* (9), 843−855.

(30) Cheng, T.; Pan, Y.; Hao, M.; Wang, Y.; Bryant, S. H. PubChem applications in drug discovery: a bibliometric analysis. *Drug discovery today* **2014**, *19* (11), 1751−1756.

(31) Liu, Y.; Li, Q.; Shao, C.; She, Y.; Zhou, H.; Guo, Y.; An, H.; Wang, T.; Yang, J.; Wan, H. Exploring the Potential Mechanisms of Guanxinshutong Capsules in Treating Pathological Cardiac Hypertrophy based on Network Pharmacology, Computer-Aided Drug Design, and Animal Experiments. *ACS omega* **2024**, *9* (16), 18083−18098.

(32) Abraham, M. J.; Murtola, T.; Schulz, R.; Páll, S.; Smith, J. C.; Hess, B.; Lindahl, E. GROMACS: High performance molecular simulations through multi-level parallelism from laptops to supercomputers. *SoftwareX* **2015**, *1*, 19−25.

(33) Valdés-Tresanco, M. S.; Valdés-Tresanco, M. E.; Valiente, P. A.; Moreno, E. gmx_MMPBSA: a new tool to perform end-state free energy calculations with GROMACS. *J. Chem. Theory Comput.* **2021**, *17* (10), 6281−6291.

(34) Chandrasekaran, B.; Abed, S. N.; Al-Attraqchi, O.; Kuche, K.; Tekade, R. K. Computer-aided prediction of pharmacokinetic (ADMET) properties. In *Dosage form design parameters*; Elsevier, 2018; pp 731−755.

(35) Pires, D. E.; Blundell, T. L.; Ascher, D. B. pkCSM: predicting small-molecule pharmacokinetic and toxicity properties using graph-based signatures. *Journal of medicinal chemistry* **2015**, *58* (9), 4066−4072.

(36) Ojha, N.; Dhamoon, A. S. Myocardial infarction. In *StatPearls [Internet]*; StatPearls Publishing, 2023.

(37) Guo, Q.; Wang, J.; Ni, C.; Pan, J.; Zou, J.; Shi, Y.; Sun, J.; Zhang, X.; Wang, D.; Luan, F. Research progress on the natural products in the intervention of myocardial infarction. *Front. Pharmacol.* **2024**, *15*, No. 1445349.

(38) Pinilla-González, V.; Rojas-Solé, C.; Gómez-Hevia, F.; González-Fernández, T.; Cereceda-Cornejo, A.; Chichiarelli, S.; Saso, L.; Rodrigo, R. Tapping into Nature's Arsenal: Harnessing the Potential of Natural Antioxidants for Human Health and Disease Prevention. *Foods* **2024**, *13* (13), 1999.

(39) Dong, L.-Y.; Chen, F.; Xu, M.; Yao, L.-P.; Zhang, Y.-J.; Zhuang, Y. Quercetin attenuates myocardial ischemia-reperfusion injury via downregulation of the HMGB1-TLR4-NF-κB signaling pathway. *Am. J. Transl. Res.* **2018**, *10* (5), 1273.

(40) Albadrani, G. M.; BinMowyna, M. N.; Bin-Jumah, M. N.; El−Akabawy, G.; Aldera, H.; AL-Farga, A. M. Quercetin prevents myocardial infarction adverse remodeling in rats by attenuating TGF-β1/Smad3 signaling: Different mechanisms of action. *Saudi J. Biol. Sci.* **2021**, *28* (5), 2772−2782.

(41) Buwa, C. C.; Mahajan, U. B.; Patil, C. R.; Goyal, S. N. Apigenin attenuates β-receptor-stimulated myocardial injury via safeguarding cardiac functions and escalation of antioxidant defence system. *Cardiovascular toxicology* **2016**, *16*, 286−297.

(42) Song, D.-K.; Jang, Y.; Kim, J. H.; Chun, K.-J.; Lee, D.; Xu, Z. Polyphenol (−)-epigallocatechin gallate during ischemia limits infarct size via mitochondrial KATP channel activation in isolated rat hearts. *Journal of Korean medical science* **2010**, *25* (3), 380−386.

(43) He, Y.; Lu, X.; Chen, T.; Yang, Y.; Zheng, J.; Chen, C.; Zhang, Y.; Lei, W. Resveratrol protects against myocardial ischemic injury via the inhibition of NF-κB-dependent inflammation and the enhancement of antioxidant defenses. *Int. J. Mol. Med.* **2021**, *47* (3), 1−1.

(44) An, N.; Zhang, G.; Li, Y.; Yuan, C.; Yang, F.; Zhang, L.; Gao, Y.; Xing, Y. Promising Antioxidative Effect of Berberine in Cardiovascular Diseases. *Front. Pharmacol.* **2022**, *13*, No. 865353.

(45) Zhang, M.; Feng, L.; Li, J.; Chen, L. Therapeutic Potential and Mechanisms of Berberine in Cardiovascular Disease. *Current Pharmacology Reports* **2016**, *2* (6), 281−292.

(46) Liu, A.; Zhang, B.; Zhao, W.; Tu, Y.; Li, J. Catalpol ameliorates psoriasis-like phenotypes via SIRT1 mediated suppression of NF-κB and MAPKs signaling pathways. *Bioengineered* **2020**, *12* (1), 183.

(47) Zhang, A.; Hao, S.; Bi, J.; Bao, Y.; Zhang, X.; An, L.; Jiang, B. Effects of catalpol on mitochondrial function and working memory in mice after lipopolysaccharide-induced acute systemic inflammation. *Experimental & Toxicologic Pathology* **2009**, *61* (5), 461−469.

(48) Zou, G.; Zhong, W.; Wu, F.; Wang, X.; Liu, L. Inhibition of lncRNA Neat1 by catalpol via suppressing transcriptional activity of NF-κB attenuates cardiomyocyte apoptosis. *Cell cycle (Georgetown, Tex.)* **2019**, *18* (24), 3432−10.

(49) Algoet, M.; Janssens, S.; Himmelreich, U.; Gsell, W.; Pusovnik, M.; Van den Eynde, J.; Oosterlinck, W. Myocardial ischemia-reperfusion injury and the influence of inflammation. *Trends in cardiovascular medicine* **2023**, *33* (6), 357−366.

(50) Toldo, S.; Mauro, A. G.; Cutter, Z.; Abbate, A. Inflammasome, pyroptosis, and cytokines in myocardial ischemia-reperfusion injury. *American Journal of Physiology-Heart and Circulatory Physiology* **2018**, *315* (6), H1553−H1568.

(51) Wu, Q.; Xu, R.; Zhang, K.; Sun, R.; Yang, M.; Li, K.; Liu, H.; Xue, Y.; Xu, H.; Guo, Y. Characterization of early myocardial inflammation in ischemia-reperfusion injury. *Front. Immunol.* **2023**, *13*, No. 1081719.

(52) Ge, H.; Lin, W.; Lou, Z.; Chen, R.; Shi, H.; Zhao, Q.; Lin, Z. Catalpol alleviates myocardial ischemia reperfusion injury by activating the Nrf2/HO-1 signaling pathway. *Microvascular Research* **2022**, *140*, No. 104302.

(53) Nemmar, A.; Beegam, S.; Zaaba, N. E.; Alblooshi, S.; Alseiari, S.; Ali, B. H. The salutary effects of catalpol on diesel exhaust particles-induced thrombogenic changes and cardiac oxidative stress, inflammation and apoptosis. *Biomedicines* **2022**, *10* (1), 99.

(54) Casciaro, M.; Di Salvo, E.; Brizzi, T.; Rodolico, C.; Gangemi, S. Involvement of miR-126 in autoimmune disorders. *Clin. Mol. Allergy* **2018**, *16*, 1−6.

(55) Chen, L.; Wang, J.; Wang, B.; Yang, J.; Gong, Z.; Zhao, X.; Zhang, C.; Du, K. MiR-126 inhibits vascular endothelial cell apoptosis through targeting PI3K/Akt signaling. *Annals of Hematology* **2016**, *95* (3), 365−374.

(56) Gao, S.; Gao, H.; Dai, L.; Han, Y.; Lei, Z.; Wang, X.; Chang, H.; Liu, S.; Wang, Z.; Tong, H.; Wu, H. miR-126 regulates angiogenesis in myocardial ischemia by targeting HIF-1 alpha. *Exp. Cell Res.* **2021**, *409* (2), No. 112925.

(57) Ren, Y.; Bao, R.; Guo, Z.; Kai, J.; Cai, C. G.; Li, Z. miR-126−5p regulates H9c2 cell proliferation and apoptosis under hypoxic conditions by targeting IL-17A. *Exp. Ther. Med.* **2020**, *21* (1), 1−1.

(58) Liu, Q.; Xiao, S.; Xia, Y. TWEAK/Fn14 activation participates in skin inflammation. *Mediators Inflammation* **2017**, *2017* (1), 1.

(59) Xiao, G.; Lyu, M.; Wang, Y.; He, S.; Liu, X.; Ni, J.; Li, L.; Fan, G.; Han, J.; Gao, X.; Wang, X.; Zhu, Y. Ginkgo Flavonol Glycosides or Ginkgolides Tend to Differentially Protect Myocardial or Cerebral Ischemia−Reperfusion Injury via Regulation of TWEAK-Fn14 Signaling in Heart and Brain. *Front. Pharmacol.* **2019**, *10*, 735.

(60) Guan, X. X.; Yang, H. H.; Zhong, W. J.; Duan, J. X.; Zhang, C. Y.; Jiang, H. L.; Xiang, Y.; Zhou, Y.; Guan, C. X. Fn14 exacerbates acute lung injury by activating the NLRP3 inflammasome in mice. *Mol. Med.* **2022**, *28* (1), 85.

(61) Kwon, O.-H.; Kim, J. H.; Kim, S.-Y.; Kim, Y. S. TWEAK/Fn14 signaling mediates gastric cancer cell resistance to 5-fluorouracil via NF-κB activation. *International journal of oncology* **2014**, *44* (2), 583−590.

(62) Tak, P. P.; Firestein, G. S. NF-κB in defense and disease NF-κB: a key role in inflammatory diseases. *J. Clin. Invest.* **2001**, *107* (1), 7−11.

(63) Wang, P.; Sun, Z. Y.; Zhang, G. Y.; Jin, Y.; Sun, W. L.; Zhao, B. S.; Chen, X.; Li, Q. B. Regulation of the NF-κB/NLRP3 signalling pathway by Shenghui Yizhi decoction reduces neuroinflammation in mice with Alzheimer's disease. *Annals of Medicine* **2024**, *56*, No. 2411011.

(64) Páll, S.; Zhmurov, A.; Bauer, P.; Abraham, M.; Lindahl, E. Heterogeneous Parallelization and Acceleration of Molecular Dynamics Simulations in GROMACS. *J. Chem. Phys.* **2020**, No. 134110.